iScience

CellPress
OPEN ACCESS

Article

The deformation of short-range order leading to rearrangement of topological network structure in zeolitic imidazolate framework glasses

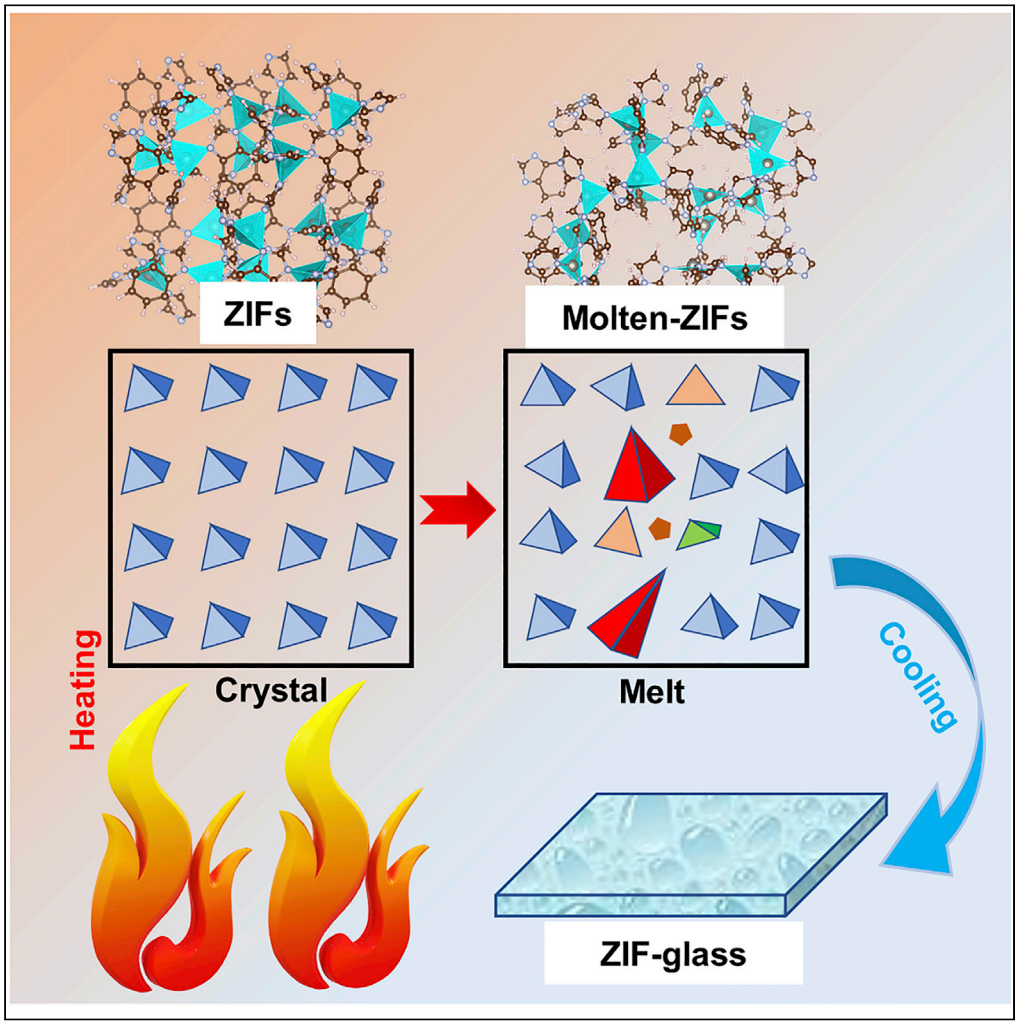

Zuhao Shi, Arramel Arramel, Thomas Douglas Bennett, Yuanzheng Yue, Neng Li

lineng@whut.edu.cn

Highlights

The ZIFs melting processes were studied by *ab initio* molecular dynamics simulation

Changes in short-range order (SRO) of molten ZIFs are investigated

Revealing the asymmetric distribution of bIm groups leads to the difference in SRO

The SRO of ZIFs can be used to compare the amorphous formation abilities

Shi et al., iScience 25, 104351
June 17, 2022
https://doi.org/10.1016/j.isci.2022.104351

iScience

CellPress
OPEN ACCESS

Article

The deformation of short-range order leading to rearrangement of topological network structure in zeolitic imidazolate framework glasses

Zuhao Shi,[1,2] Arramel Arramel,[3] Thomas Douglas Bennett,[4] Yuanzheng Yue,[1,5] and Neng Li[1,2,6,7,*]

SUMMARY

In recent years, the study of the glassy structure of zeolitic imidazolate frameworks (ZIFs) has been a key breakthrough in glass science. Yet the theoretical understanding of the structure of these complex materials is still in its infancy, especially the short-range structure. The short-structural disorder of two ZIFs and their corresponding molten structure, namely, ZIF-4 and ZIF-62 are studied, using *ab initio* simulations. Changes in short-range order are investigated, particularly the changes in bond length, bond angle, and tetrahedral unit volume. Furthermore, the asymmetric distribution of organic groups caused by the benzimidazole functional group leads to the difference in short-range disorder between ZIF-4 and ZIF-62 glasses, which contribute to the glass-forming ability difference.

INTRODUCTION

As a subclass of the diverse metal–organic frameworks (MOFs) family, zeolitic imidazolate frameworks (ZIFs) structures have attracted much attention in recent years (Chen et al., 2014; Zhao et al., 2017). Structural disorder, in particular, is an emerging topic in the MOF fields (Hou et al., 2019; To et al., 2020; Wang et al., 2020; Zhou et al., 2018) that is still at an early stage. Glasses formed by melt-quenching ZIFs are regarded as a new type of glass, because of the linked organic-inorganic hybrid structure which is significantly different from the traditional glass structure based on their delicate composition (Bennett and Horike, 2018; Bennett et al., 2015; Widmer et al., 2019). Among various ZIFs glasses, considerable efforts have been devoted to ZIF-4 ($Zn[Im]_2$, Im = imidazolate, $C_3H_3N_2^-$) and ZIF-62 ($Zn[Im_{1.75}bIm_{0.25}]$, bIm = benzimidazolate, $C_7H_5N_2^-$) glasses. Both crystalline structures of ZIF-4 and ZIF-62 have similar cag topologies (Gustafsson and Zou, 2013; Park et al., 2006).

Thermophysical properties and structural differences between the two structures at high temperatures have previously been observed in experiments. The melting temperature of ZIF-62 (T_m = 710 K) is lower than that of ZIF-4 (T_m = 863 K) which the addition of an electron-donating benzene ring to the imidazolate anion is accompanied by a decrease in melting point (Bennett et al., 2016). Further experiments have demonstrated that the ZIF-62 melting point increases with increasing bIm functional groups (Frentzel-Beyme et al., 2019). Meanwhile, the long melting time (melting time >30 min) observed in the production of ZIF-62 glass can be attributed to the partial decomposition during melting (Stepniewska et al., 2020). The ZIF-62 has been confirmed to exhibit higher glass-forming ability (GFA) than ZIF-4 and any other systems that can be melted, owing to the higher steric hindrance and frustrated network dynamics in ZIF-62 (Madsen et al., 2020; Qiao et al., 2018).

Some studies have also been carried out to reveal differences in the chemical or electronic structure of the amorphous ZIFs through simulations (Adhikari et al., 2016; Baral et al., 2017; Cimas et al., 2014; Li et al., 2020; Xiong et al., 2020a, 2020b). However, it remains challenging to establish a connection between the physical properties, local topology, and the underlying chemistry of glasses (Ma and Horike, 2022). One of the most striking studies comes from the work by Gaillac et al., which provides an in-depth description of liquid ZIFs at high temperatures (Gaillac et al., 2017, 2018). In particular, the simulated thermodynamic study of the imidazolate exchange event in the molten state bridges the gap of *in situ* observing the reaction process due to disordered structures and high temperatures. This inspires us whether it is

[1]State Key Laboratory of Silicate Materials for Architectures, Wuhan University of Technology, Wuhan 430070, China

[2]Shenzhen Research Institute of Wuhan University of Technology, Shenzhen 518000, China

[3]Department of Physics, National University of Singapore, 2 Science Drive 3, Singapore 117551 Singapore

[4]Department of Materials Science and Metallurgy, University of Cambridge, 27 Charles Babbage Road, Cambridge CB3 0FS, UK

[5]Department of Chemistry and Bioscience, Aalborg University, 9220 Aalborg, Denmark

[6]State Center for International Cooperation on Designer Low-Carbon and Environmental Materials (CDLCEM), School of Materials Science and Engineering, Zhengzhou University, Zhengzhou 450001, Henan, China

[7]Lead contact

*Correspondence: lineng@whut.edu.cn

https://doi.org/10.1016/j.isci.2022.104351

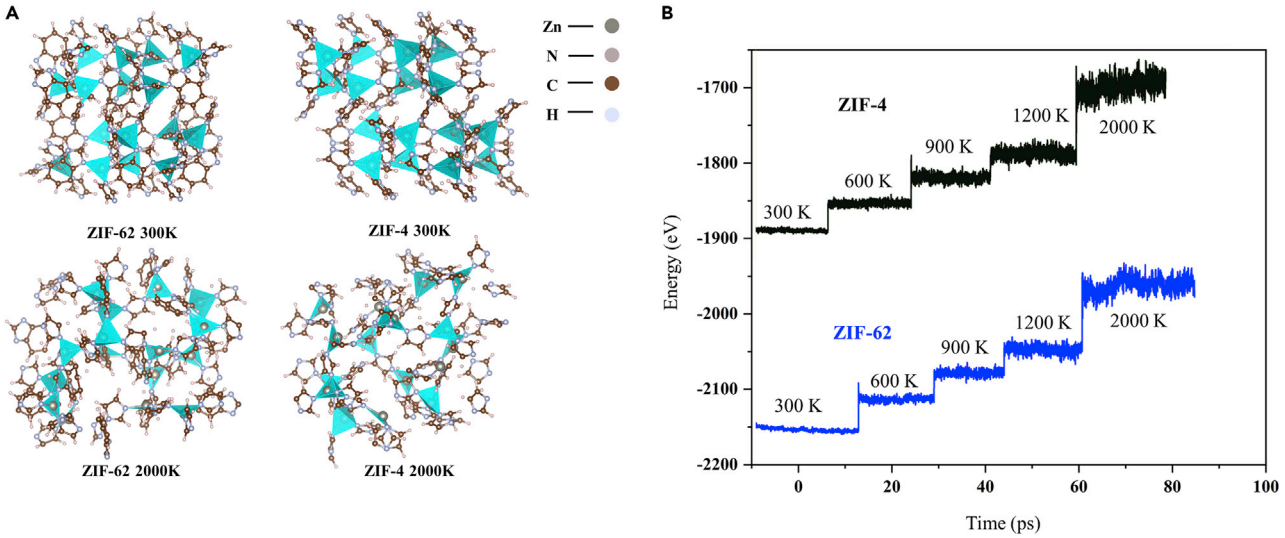

Figure 1. Structure of crystal and molten structures of ZIFs

(A) The structures of ZIF-62 and ZIF-4 in 300 K and 2000 K. Gray – Zn atoms; Blue – N atoms, Brown – C atoms, White – H atoms.

(B) The average energy change of ZIF-62 and ZIF-4 in simulation. The black line and blue line represent the energy of ZIF-4 and ZIF-62, respectively.

possible to build on their work and explain the differences in the GFA of ZIF-4 and ZIF-62, through consideration of their structural variability in the molten state?

In this work, we compare in detail the similarities and differences between molten ZIF-4 and ZIF-62, in terms of structural changes in the short range (SR) and midrange (MR) during melting. We confirmed the steric hindrance effect of the bIm group on the kinetics of the melting process. Meanwhile, the difference in GFA between the two is also explained about the percolation model of the glass transition (T_g).

RESULTS

In the work, the dynamic simulations were carried out at varying temperatures (300 K, 600 K, 900 K, 1200 K, and 2000 K) to investigate the structures of the ZIFs in the molten state. The structures of ZIF-4 and ZIF-62 in the temperature of 300 K (crystalline state) and 2000 K (molten state) are shown in Figures 1A and 1B displays the average energy variation based on our simulations. For ZIF-4, its internal energy increases from −1789.22 eV at 300K to −1751.62 eV at 2000K. For ZIF-62, its internal energy values at 300 and 2000K are −2148.62 eV and −2048.38 eV, respectively.

It turns out that the energy of the structure increases with the increase in temperature because of the metastable molten state. By comparing the structures probed at 300 K and 2000 K, we found the collapse of the original cag structure, which indicted a salient structural rearrangement in the medium range (MR). Of more interest to us are the changes in the short-range structure. In ZIFs, the basic unit constituting the short-range structure is the [ZnN_4] tetrahedron. We describe this short-range structure in terms of the distribution of bond angles, the variation in tetrahedral volume, and the coordination number of the central Zn atoms. The statistics of the N-Zn-N bond angle and the volume of the [ZnN_4] structural unit are plotted in Figures 2 and 3, with the average values listed in Table 1. For the equilibrium structure at different temperatures, the Python was used to calculate and statistically analyze the bond angle distribution of N-Zn-N, and hence, to directly reflect the distortion of the Zn^{2+} coordination environment under the influence of temperature (Robinson et al., 1971).

Figure 2 shows the distribution of the different value of N-Zn-N bond angles in ZIF-62 and ZIF-4 as temperature rises. In the crystal ZIF-4, the N-Zn-N bond angle in the [ZnN_4] tetrahedra is 109°28′, which is consistent with the central angle of the orthotetrahedron. At room temperature (300 K), the angle distribution values deviate a little due to thermal vibrations of the atoms but mostly lie between 100° and 120°. As shown in Figure 2, the proportion of N-Zn-N bond angles in 100°–120° at 300 K is 91.8% and 92.8%, for

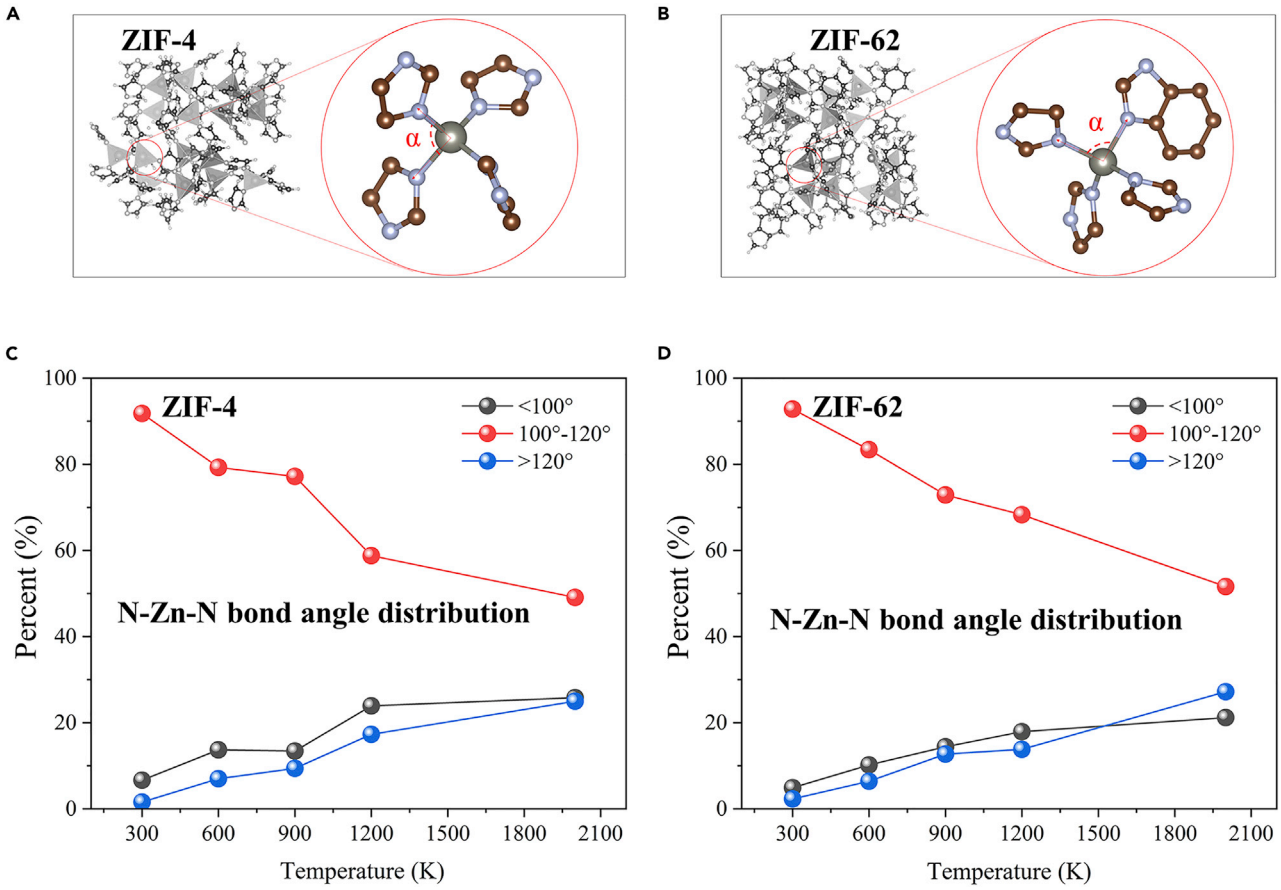

Figure 2. Distribution of bond angle in ZIF-4 and ZIF-62

Local structure of N-Zn-N bond angle in (A) ZIF-4 and (B) ZIF-62; N-Zn-N bond angle distribution in (C) ZIF-4 and (D) ZIF-62 with various temperature.

ZIF-4 and ZIF-62, respectively. There is a difference (about 0.46°) in N-Zn-N angle ($\Delta\theta$) between ZIF-4 and -62 at 300 K because of the asymmetric distribution of the bIm groups in ZIF-62.

As the temperature rises, part of the N-Zn-N angle begins to become smaller as well as the other part becomes larger, reflecting the distortion of the tetrahedron. At 900 K and even higher temperatures, the average $\Delta\theta$ between the two ZIFs is found to be about 0.1°. Moreover, the difference in bond angle distribution between two ZIFs is significantly reduced with increasing temperature. In the molten state (2000 K), only 49.1% and 51.6% of the N-Zn-N bond angles in ZIF-4 and ZIF-62, respectively, were in the range of 100°–120°, with the remainder all undergoing angular changes. Therefore, we infer that a short-range disorder can be associated with the wide angular distribution within the studied temperature regime. This inference agrees with the experimental results (Madsen et al., 2020).

In addition to the N-Zn-N bond angle, we also investigate the volume of [ZnN_4] tetrahedron to describe another form of disorder in SR. We use python to analyze the volume change of [ZnN_4] tetrahedron in ZIFs at 300 K, 600 K, 900 K,1200 K, and 2000 K. It is important to note that the volume of [ZnN_4] does not exist, but can be seen as an indicator of the degree of tetrahedral ordering on the short-range structure. In the crystalline state (300 K), the volume of [ZnN_4] tetrahedron is totally in the range of 23–25 $Å^3$. As the temperature rises, the volume of the basic tetrahedron for both ZIF-4 and ZIF-62 exhibits a rapid change, reflecting the deformation which occurs, as shown in Figure 3. The proportion of [ZnN_4] volumes between 23 and 25$Å^3$ decreases with increasing temperature. The thermal vibrations of the atoms near the equilibrium position lead to an elongation in bond lengths and distortion bond angles, which is the main reason for variations in volume.

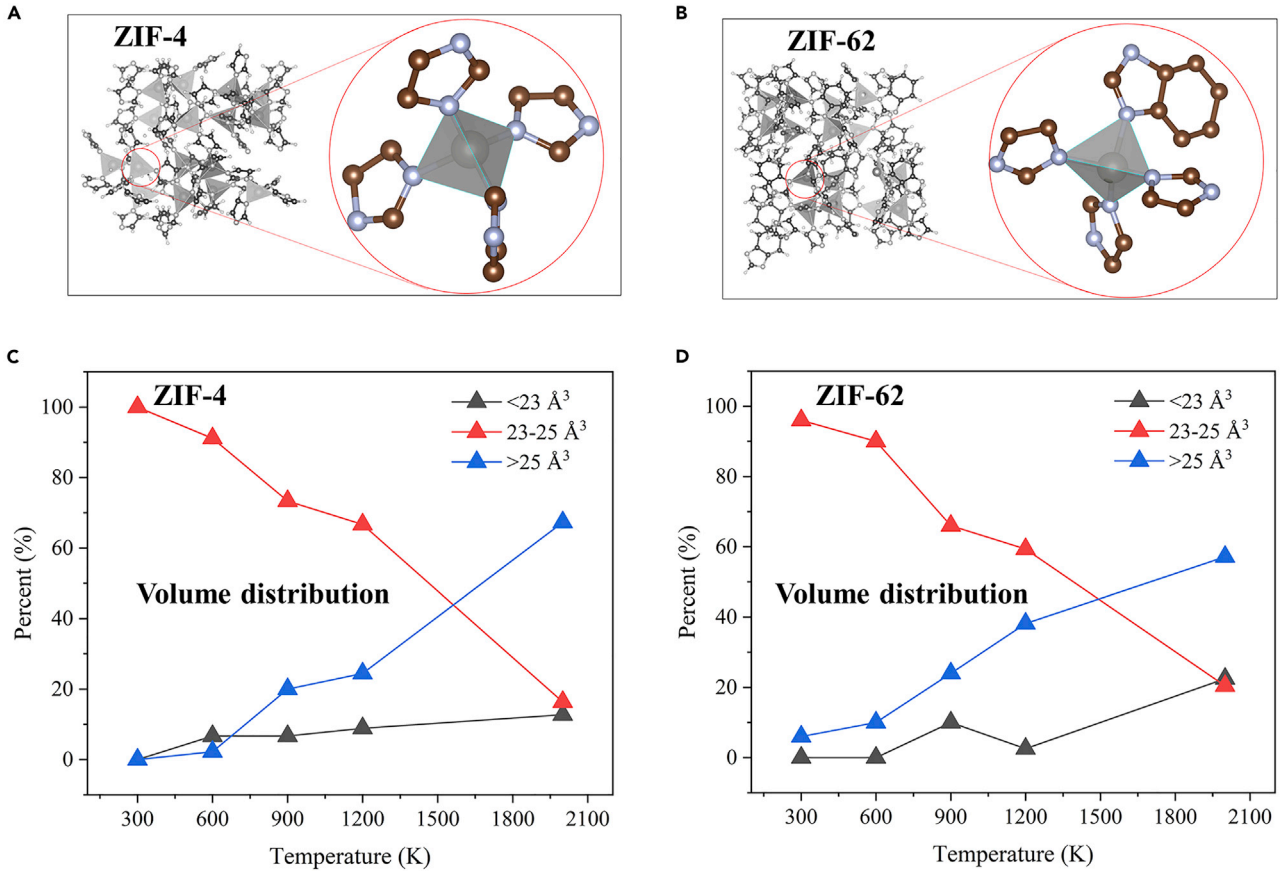

Figure 3. Distribution of tetrahedron volume in ZIF-4 and ZIF-62

Local structure of [ZnN_4] in (A) ZIF-4 and (B) ZIF-62; [ZnN_4] Volume distribution in (C) ZIF-4 and (D) ZIF-62 with various temperature.

In the molten state, the increase in the volume of short-range structural tetrahedra becomes dominant, with 67.3% and 57.1% of the [ZnN_4] tetrahedra possessing a volume above 25 $Å^3$ in ZIF-4 and ZIF-62, respectively. This again demonstrates the increased disordering of the short-range structure in the molten state. The lower number of high-volume units in ZIF-62 reflects the suppression of short-range structural disorder by the "bIm" group, which we will verify later in the kinetic and thermodynamic description of defects in the molten state of two ZIFs.

The alteration of the central atomic coordination environment is the main manifestation of the difference between the crystalline and amorphous structures. In the original [ZnN_4] tetrahedron in ZIF-4 and ZIF-62, Zn atoms are typically four-coordinated N atoms in the structure. However, the Zn-N bond weakens with an increase of temperature rises since the thermally induced atomic vibration is enhanced, and thereby the bond length is extended. Figure 4A shows the Zn-N pairs radial distribution functions (PRDF) of ZIF-62 and ZIF-4 in equilibrium at different temperatures. In the 2000 K, the overlap of coattails of the first and second peaks in PRDF indicates the molten states shown here.

For high-temp PRDF, the widening of the first peak is induced by the melting process due to the substitution of the imidazolate. The renewal of the Zn-N bonds upon melting causes structural reconstruction is also confirmed by experiments and simulations (Madsen et al., 2020; Li et al., 2020b; Zeng, 2021). Figure 4B shows the scheme of the substitution of the imidazolate in ZIF-4 and ZIF-62, where the vertical axis is the distance between Zn-Im and the horizontal axis is time. The data were obtained by statistical analysis of the trajectory files, with one substitution of the imidazolate period being around 2 ps. Compared to ZIF-4, the distance between the imidazolate and the central Zn node is shorter in ZIF-62, which is due to the steric hindrance effect of the larger "bIm" group in the lattice.

Table 1. The average N-Zn-N angle and [ZnN4] volume with temperature

	$Angle_{300}$ (°)	$Angle_{600}$ (°)	$Angle_{900}$ (°)	$Angle_{1200}$ (°)
ZIF-4	108.63	108.59	109.01	108.84
ZIF-62	109.09	109.01	109.00	108.98
	$Voulme_{300}$ ($Å^3$)	$Voulme_{600}$ ($Å^3$)	$Voulme_{900}$ ($Å^3$)	$Voulme_{1200}$ ($Å^3$)
ZIF-4	25.15	24.57	25.40	25.86
ZIF-62	25.08	25.32	25.29	26.45

Inspired by Gaillac et al. (2017), we have investigated the thermodynamic changes in the melting process to compare the differences between ZIF-4 and ZIF-62 in the melting process. From the PRDF of Zn-N, we use the $F(r) = -k_B*T* \ln(r)$ to calculate the potential of mean force (PMF) between the two atoms. This can be used to calculate the energy change during the Zn-N bond length change and thus obtain thermodynamic information about this process. Figure S1 displays the PMF along with the Zinc-Nitrogen distance in variation temperature.

By using the highest energy in each PMF, the Zn-N bonds activation free energy barrier, ΔF, can be computed following a van't Hoff law $\Delta F = \Delta H - T*\Delta S$. Through this method, the enthalpy and entropy change of Zn-N bonds broken in ZIF-4 is $\Delta H \approx 164.3$ kJ/mol and $\Delta S \approx 44.1$ J/(mol*K), and in ZIF-62 is $\Delta H \approx 129.3$ kJ/mol and $\Delta S \approx 28.5$ J/(mol*K). In the 2000 K, the Gibbs energy change of melting is 76.1 kJ/mol and 72.3 kJ/mol.

By integrating the PRDF of Zn-N, we can find the coordination number of the N atom around the central Zn. According to the calculation, the average coordination number of Zn in ZIF-4 and ZIF-62 is 3.48 and 3.60, respectively, at 2000 K. We assume that the dislocation of center Zn atom is composed of three coordination of N, i.e. $[ZnN_3]$. Based on this assumption, we can roughly estimate that the proportions of undercoordinated Zn in ZIF-4 and ZIF-62 are 52% and 40%, respectively. The previous analysis of the short-range structure shows the structurally asymmetric distribution due to the bIm functional group and the spatial site-blocking role played in the substitution of the imidazolate. This results in different concentrations of defect formation in ZIF-4 and ZIF-62. In terms of quantitative distribution, 52% of the Zn atoms in ZIF-4 are in the triple coordination environment of the N atoms, compared to 40% in ZIF-62, indicating that more bonds break in the Zn-N framework of ZIF-4 in the molten state.

Figure 5 shows the structure of the simplified framework of ZIF-4 and ZIF-62 in the crystalline state and molten state. Furthermore, we try to establish a correlation between the degree of destruction of this topology and the ability to form glass, and here, we consider the configuring percolation theory (CPT) proposed by Ojovan (Ojovan, 2013; Ojovan and Lee, 2010). We simplify the structure of ZIF-4 and ZIF-62 to a network structure consisting of Zn and N atoms only. For these simplified framework structures, the main defect is the breakage of the Zn-N bonds under thermal conditions:

$$(-\mathrm{Zn}-)_{\mathrm{net}} + (-\mathrm{N}-\mathrm{N}-\mathrm{Zn})_{\mathrm{net}} \rightarrow (-\mathrm{Zn}-)_{\mathrm{defect}} + (-\mathrm{N}-\mathrm{N}-\mathrm{Zn})_{\mathrm{defect}}$$

As mentioned above, the enthalpy and entropy change of Zn-N bonds broken in ZIF-4 is $\Delta H \approx 164.3$ kJ/mol and $\Delta S \approx 44.1$ J/(mol*K), and in ZIF-62 is $\Delta H \approx 129.3$ kJ/mol and $\Delta S \approx 28.5$ J/(mol*K). According to the CPT, the glass transition temperature can be found from the condition of broken bond percolation threshold, which gives (Ojovan and Lee, 2010):

$$T_g = \frac{H_d}{S_d + R * ln[(1 - \theta_c)/\theta_c]}$$

where H_d and S_d are enthalpy and entropy of defects in melts, and θ_c is the percolation threshold. By substituting the values into the formula for the glass transition temperature of CPT, we obtain a ratio of about 0.94, which is closer to the experimental value of the ratio.

It should be noted, however, that the glass transition temperature estimated by this method is much higher than the actual value. This deviation is partly due to the percolation threshold θ, which for strong melts such as SiO_2 or GeO_2 is equal to the Scher-Zallen critical density of 0.15. However, for the complex structure of ZIFs, the formation of defects during the melting-quenching process consists of the broken Zn-N bonds.

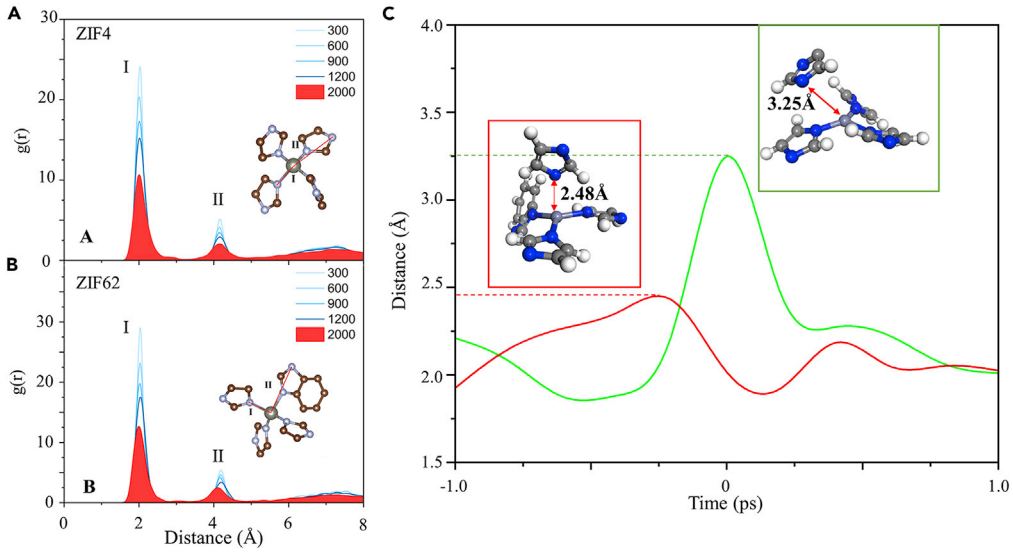

Figure 4. The local stucture of ZIF-4 and ZiF-62

Thermal decomposition of organic ligands in ZIFs PRDF of Zn-N in (A) ZIF-4 (up) and (B) ZIF-62(down); (C) Scheme of the substitution of the imidazolate in ZIF-4 (green) and ZIF-62 (red).

When considering the breakage of bonds within functional groups, and other interactions between different atoms, the corresponding percolation threshold of complex network is significantly reduced, as is the case in alkali metal-doped glass formers (Adams and Swenson, 2004). On the other hand, as ZIFs glasses are hybrid organic-inorganic structure, more correction terms may be needed to compensate for the differences in melting behavior due to the different types of interatomic bonding. In conclusion, more research is needed on the fractal structure of the molten and glassy states of ZIFs for the theoretical modeling of glass transition.

Figure 6 shows a schematic diagram describes the evolution of the short-range disorder structure of ZIFs with temperature. As temperature increases, the change in the bond length leads to the change of coordination number (N atoms) of Zn and thereby contributes to the undercoordination of center Zn atoms at high temperature. Meanwhile, the changes in the N-Zn-N bond angle and bond length cause the volume change of the [ZnN_4] tetrahedral. The variation in both coordination and tetrahedral volume changes the chemical environment at the vicinity of Zn atoms. The structural disorder around the Zn node can be detected by NMR (Madsen et al., 2020).

In addition to the tetrahedral twist, the coordination-deficient [ZnN_4] tetrahedra due to substitution of the imidazolate and the mobile imidazolate groups are among the manifestations of the short-range disorder. Interestingly, the short-range disorder degree of the structure increases with the increase of temperature, and the band gap of the corresponding structure gradually decreases (Figure S2). The correlation between disorder degree and electronic structure needs to be further studied, considering the underestimation of energy band gap by GGA functional and the exclusion of temperature effect on the electronic structure. This study provides insight into the role of the structural evolution in SR and MR in MOF glass formation.

DISCUSSION

As a new number of glass families, the research on MOF glasses would contribute to exploring ''how the long-range disorder structure was constructed from short-range order structure'', as well as to understand glass structure, glass formation, structure-properties relevance, and dynamic characters of glass (Yin et al., 2020). This work was carried out on two typical ZIFs with glass-forming ability. However, the findings of the study have implications for the glass/amorphous forming ability description of more ZIFs. Unlike conventional glass formers, such as silica dioxide, the metal-organic ligand network structure of ZIFs leads to a more complex short-range structure. Our calculations show that glass structures prepared by the melting-quenching method undergo a disordering process on the short-range structure at high

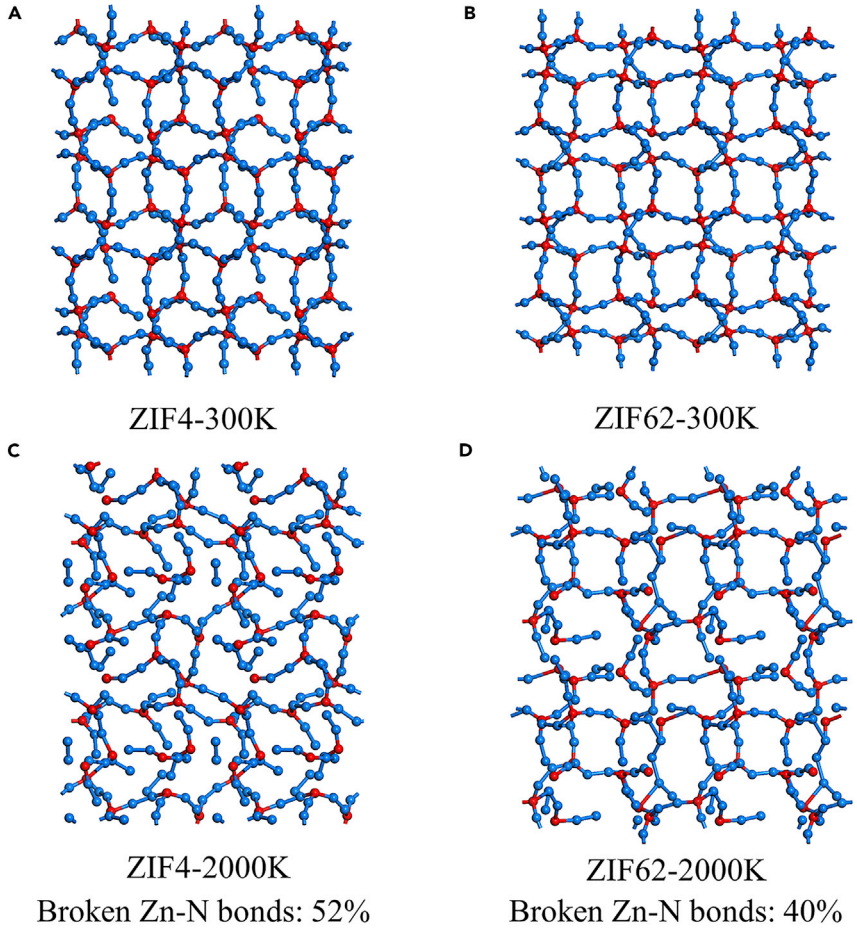

Figure 5. The Zn-N bonds percentages in ZIFs under high tempreture (A) ZIF-4@300K, (B) ZIF-62@300K, (c) ZIF-4@2000K, (D) ZIF-62@2000K

temperatures. The ease with which this disordering process occurs is related to the distribution of the short-range structure in its crystalline state. Therefore, by characterizing the short-range order of different ZIFs, combined with continuously updated experimental advances, it is able to establish a simple, paper-and-pencil calculation based on the crystal structure for a comparison of glass/amorphous formation ability.

Systematic research in this area is largely at a blank stage, and we provide an idea here as a reference, shown in Figure 7. We propose to establish a description of the amorphous/glass-forming ability based on the homogeneity and sparsity of the short-range structure distribution in the crystalline state. We collected short-range structures (<6Å) of 23 ZIFs and transformed the PRDF of Zn data into two sets of ordinal parameters, X and Y. The specific transformation methods are described in Experimental Procedures in Figure S3. X reflects the sparsity and Y reflects the uniformity of the distribution in short-range structures of the metal atoms and around organic ligands. In Figure 7, the region closer to the lower left corner indicates a denser and ordered coordination environment for Zn; the region closer to the upper left corner corresponds to a structure in which the coordination environment for Zn is dense but less ordered, with more coordination atoms stacked closer to the central Zn atom, while the region in the lower right corner corresponds to a structure that is more ordered but more sparsely distributed in space.

According to the present experimental data, ZIF-4, ZIF-62, and ZIF-76, which can form glasses, all have lower Y values, and in particular, ZIF-62, which has the best glass-forming ability, is located in the region closest to the lower left-hand corner. ZIF-8, which has extreme values on the x axis, has outstanding

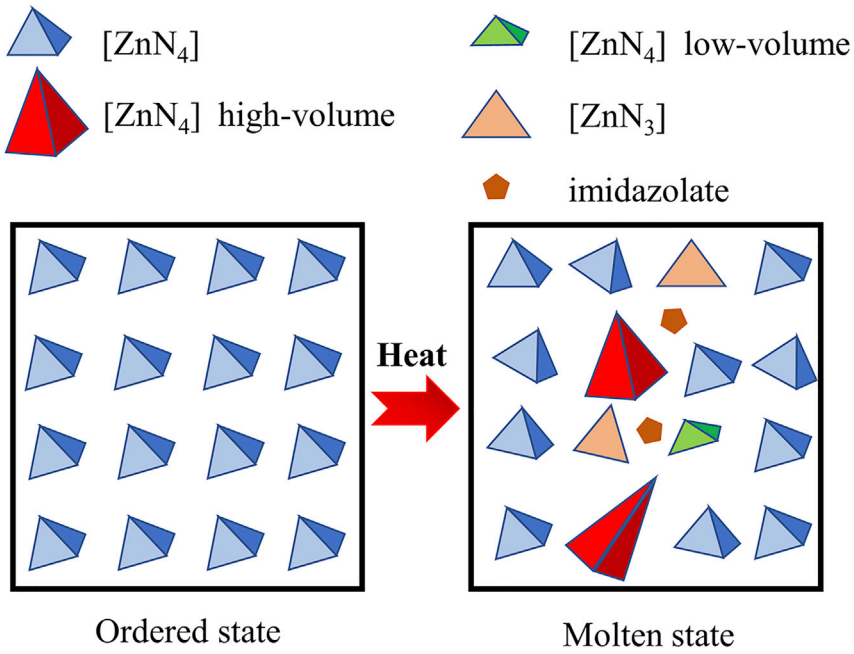

Figure 6. The evolution of the short-range disorder structure of ZIFs with temperature

flexibility in the ZIFs. It should be stated again that we are not in a position to assess and correct the accuracy of such sequential covariates any further as there is not a wealth of current data on more amorphous studies of ZIFs, and this is provided here only as an update of our work for the benefit of a wider range of researchers.

In summary, we studied the SR structure change in two classical liquid- and glass-forming ZIFs upon heating treatment via the AIMD method. The calculations show that the short-range structure of ZIFs in the molten state has a certain degree of disorder, which is reflected in the metal-ligand bond angle distribution, and the distortion of the [ZnN_4] tetrahedra. The comparison of Zn-N PRDF between the two ZIFs indicates that the coordination environment of the [ZnN_4] tetrahedron varies upon melting. The fraction of the non-equilibrium Zn coordination of ZIF-4 is up to 52%, and in contrast, in the ZIF-62, this percentage is only 40%. The transfer of Im functional groups due to heat fluctuation in ZIFs is inhibited due to the steric hindrance effect of the bIm functional group. This results in the differences in thermodynamic characteristics of the defects in the two structures.

Limitations of the study

The correlation between the evolutionary features of the short procedure and the experimental thermodynamic characteristics of the amorphization process of ZIF has also yet to be discussed in more depth. Furthermore, the simulation of complex system evolutionary processes in larger scales remains difficult, considering that the AIMD method in this paper is very costly.

STAR★METHODS

Detailed methods are provided in the online version of this paper and include the following:

- KEY RESOURCES TABLE
- RESOURCE AVAILABILITY
  - Lead contact
  - Materials availability
  - Data and code availability
- EXPERIMENTAL MODEL AND SUBJECT DETAILS
- METHOD DETAILS

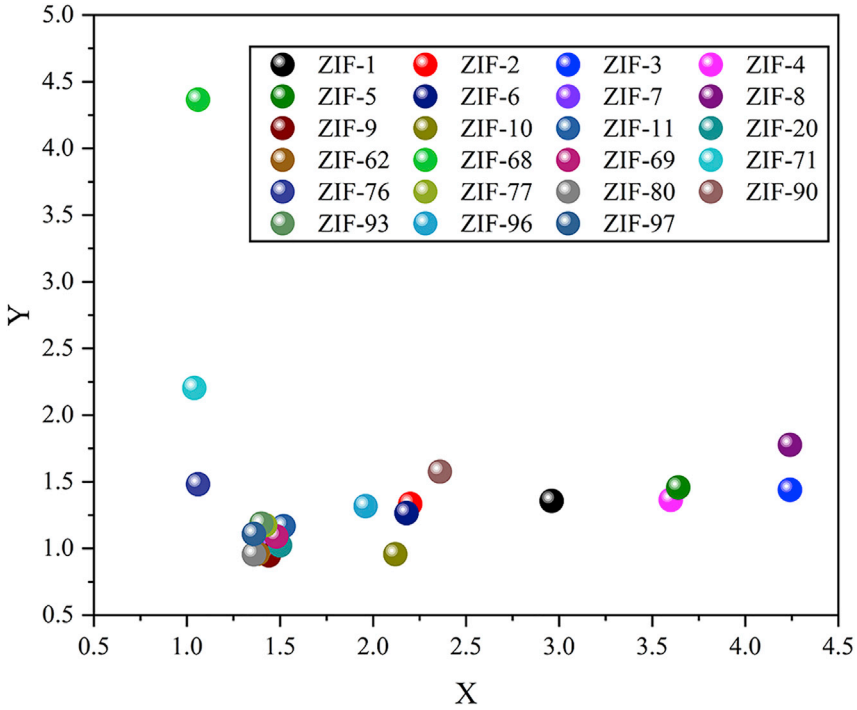

Figure 7. The X/Y relationship of 23 ZIFs

- QUANTIFICATION AND STATISTICAL ANALYSIS
- ADDITIONAL RESOURCES

SUPPLEMENTAL INFORMATION

Supplemental information can be found online at https://doi.org/10.1016/j.isci.2022.104351.

ACKNOWLEDGMENTS

This work was supported by the National Key Research and Development Plan of China (project 2019YFC1904901), the Natural Science Fund for Distinguished Young Scholars of Hubei Province (No. 2020CFA087); Guangdong Basic and Applied Basic Research Foundation (No. 2022A1515011303); the Fok Ying Tong Education Foundation for Young Teachers in the Higher Education Institutions of China (No. 161008); the Basic Research Program of Shenzhen (No. JCYJ20190809120015163); the central government guides local science and technology development funds to freely explore basic research projects (2021Szvup106); the Overseas Expertise Introduction Project for Discipline Innovation of China (No. B18038), and Fundamental Research Funds for the Central Universities (WUT20163064). T.D.B. acknowledges the Royal Society for a University Research Fellowship (UF150021), the Leverhulme Trust for a Philip Leverhulme Prize and the University of Canterbury Te Whare Wānanga o Waitaha, New Zealand, for a University of Cambridge Visiting Canterbury Fellowship.

AUTHOR CONTRIBUTIONS

N L. conceived the project and designed the calculations. Z.H.S. conducted the density functional theory calculations. Z.H.S., N.L., and T.D.B. analyzed the data and discussed the results. Z.H.S., N.L., A.A., T.D.B., and Y.Z.Y. wrote the manuscript. All authors reviewed and contributed to the final manuscript.

DECLARATION OF INTERESTS

The authors declare no competing interests.

Received: February 2, 2022
Revised: March 22, 2022
Accepted: April 28, 2022
Published: June 17, 2022

REFERENCES

Adams, S., and Swenson, J. (2004). Structure conductivity correlation in reverse Monte Carlo models of single and mixed alkali glasses. Solid State Ion. *175*, 665–669. https://doi.org/10.1016/j.ssi.2004.08.038.

Adhikari, P., Xiong, M., Li, N., Zhao, X., Rulis, P., and Ching, W.Y. (2016). Structure and electronic properties of a continuous random network model of an amorphous zeolitic imidazolate framework (a-ZIF). J. Phys. Chem. C *120*, 15362–15368. https://doi.org/10.1021/acs.jpcc.6b06337.

Baral, K., Li, A., and Ching, W.Y. (2017). Ab initio modeling of structure and properties of single and mixed alkali silicate glasses. J. Phys. Chem. A *121*, 7697–7708. https://doi.org/10.1021/acs.jpca.7b06530.

Bennett, T.D., and Horike, S. (2018). Liquid, glass and amorphous solid states of coordination polymers and metal-organic frameworks. Nat. Rev. Mater. *3*, 431–440. https://doi.org/10.1038/s41578-018-0054-3.

Bennett, T.D., Tan, J.C., Yue, Y.Z., Baxter, E., Ducati, C., Terrill, N.J., Yeung, H.H.M., Zhou, Z.F., Chen, W.L., Henke, S., et al. (2015). Hybrid glasses from strong and fragile metal-organic framework liquids. Nat. Commun. *6*, 8079. https://doi.org/10.1038/ncomms9079.

Bennett, T.D., Yue, Y.Z., Li, P., Qiao, A., Tao, H.Z., Greaves, N.G., Richards, T., Lampronti, G.I., Redfern, S.A.T., Blanc, F., et al. (2016). Melt-quenched glasses of metal-organic frameworks. J. Am. Chem. Soc. *138*, 3484–3492. https://doi.org/10.1021/jacs.5b13220.

Blöchl, P.E. (1994). Projector augmented-wave method. Phys. Rev. B *50*, 17953–17979. https://doi.org/10.1103/physrevb.50.17953.

Chen, B.L., Yang, Z.X., Zhu, Y.Q., and Xia, Y.D. (2014). Zeolitic imidazolate framework materials: recent progress in synthesis and applications. J. Mater. Chem. A *2*, 16811–16831. https://doi.org/10.1039/c4ta02984d.

Cimas, A., Tielens, F., Sulpizi, M., Gaigeot, M.P., and Costa, D. (2014). The amorphous silica-liquid water interface studied by ab initio molecular dynamics (AIMD): local organization in global disorder. J. Phys. Condens. Matter. *26*, 244106. https://doi.org/10.1088/0953-8984/26/24/244106.

Frentzel-Beyme, L., Kloß, M., Kolodzeiski, P., Pallach, R., and Henke, S. (2019). Meltable mixed-linker zeolitic imidazolate frameworks and their microporous glasses: from melting point engineering to selective hydrocarbon sorption. J. Am. Chem. Soc. *141*, 12362–12371. https://doi.org/10.1021/jacs.9b05558.

Gaillac, R., Pullumbi, P., Beyer, K.A., Chapman, K.W., Keen, D.A., Bennett, T.D., and Coudert, F.X. (2017). Liquid metal-organic frameworks. Nat. Mater. *16*, 1149–1154. https://doi.org/10.1038/nmat4998.

Gaillac, R., Pullumbi, P., and Coudert, F.X. (2018). Melting of zeolitic imidazolate frameworks with different topologies: insight from first-principles molecular dynamics. J. Phys. Chem. C *122*, 6730–6736. https://doi.org/10.1021/acs.jpcc.8b00385.

Grimme, S., Antony, J., Ehrlich, S., and Krieg, H. (2010). A consistent and accurate ab initio parametrization of density functional dispersion correction (DFT-D) for the 94 elements H-Pu. J. Chem. Phys. *132*, 154104. https://doi.org/10.1063/1.3382344.

Gustafsson, M., and Zou, X.D. (2013). Crystal formation and size control of zeolitic imidazolate frameworks with mixed imidazolate linkers. J. Porous Mater. *20*, 55–63. https://doi.org/10.1007/s10934-012-9574-1.

Hafner, J. (2008). Ab-initio simulations of materials using VASP: density-functional theory and beyond. J. Comput. Chem. *29*, 2044–2078. https://doi.org/10.1002/jcc.21057.

Hoover, W.G. (1985). Canonical dynamics: equilibrium phase-space distributions. Phys. Rev. A Gen. Phys. *31*, 1695–1697. https://doi.org/10.1103/physreva.31.1695.

Hou, J.W., Ashling, C.W., Collins, S.M., krajnc, A., Zhou, C., Longley, L., Johnstone, D.N., Chater, P.A., Li, S.C., Coulet, M.V., et al. (2019). Metal-organic framework crystal-glass composites. Nat. Commun. *10*, 2580. https://doi.org/10.1038/s41467-019-10470-z.

Humphrey, W., Dalke, A., and Schulten, K. (1996). VMD: visual molecular dynamics. J. Mol. Graph. *14*, 33–38. https://doi.org/10.1016/0263-7855(96)00018-5.

Li, N., Blankson, K., Yang, Y., Zhang, P., and Zhao, X. (2020). Unraveling the electronic structure, mechanical, and dielectric properties of ZnPurBr-MOF: ab initio calculations. APL Mater. *8*, 111101. https://doi.org/10.1063/5.0022647.

Ma, N., and Horike, S. (2022). Metal-organic network-forming glasses. Chem. Rev. *122*, 4163–4203. https://doi.org/10.1021/acs.chemrev.1c00826.

Madsen, R.S.K., Qiao, A., Sen, J.N., Hung, I., Chen, K.Z., Gan, Z.H., Sen, S., and Yue, Y.Z. (2020). Ultrahigh-field ^{67}Zn NMR reveals short-range disorder in zeolitic imidazolate framework glasses. Science *367*, 1473–1476. https://doi.org/10.1126/science.aaz0251.

Momma, K., and Izumi, F. (2011). VESTA 3 for three-dimensional visualization of crystal, volumetric and morphology data. J. Appl. Crystallogr. *44*, 1272–1276. https://doi.org/10.1107/s0021889811038970.

Nosé, S. (1984). A unified formulation of the constant temperature molecular dynamics methods. J. Chem. Phys. *81*, 511–519. https://doi.org/10.1063/1.447334.

Ojovan, M.I. (2013). Ordering and structural changes at the glass-liquid transition. J. Non-Cryst. Solids *382*, 79–86. https://doi.org/10.1016/j.jnoncrysol.2013.10.016.

Ojovan, M.I., and Lee, W.B.E. (2010). Connectivity and glass transition in disordered oxide systems. J. Non-Cryst. Solids *356*, 2534–2540. https://doi.org/10.1016/j.jnoncrysol.2010.05.012.

Park, K.S., Ni, Z., Côté, A.P., Choi, J.Y., Huang, R., Uribe-Romo, F.J., Chae, H.K., O'Keeffe, M., and Yaghi, O.M. (2006). Exceptional chemical and thermal stability of zeolitic imidazolate frameworks. Proc. Natl. Acad. Sci. U S A *103*, 10186–10191. https://doi.org/10.1073/pnas.0602439103.

Perdew, J.P., Burke, K., and Ernzerhof, M. (1996). Generalized gradient approximation made simple. Phys. Rev. Lett. *77*, 3865–3868. https://doi.org/10.1103/physrevlett.77.3865.

Qiao, A., Bennett, T.D., Tao, H.Z., Krajnc, A., Mali, G., Doherty, C.M., Thornton, A.W., Mauro, J.C., Greaves, G.N., and Yue, Y.Z. (2018). A metal-organic framework with ultrahigh glass-forming ability. Sci. Adv. *4*, eaao6827. https://doi.org/10.1126/sciadv.aao6827.

Robinson, K., Gibbs, G.V., and Ribbe, P.H. (1971). Quadratic elongation: a quantitative measure of distortion in coordination polyhedra. Science *172*, 567–570. https://doi.org/10.1126/science.172.3983.567.

Stepniewska, M., Ostergaard, M.B., Zhou, C., and Yue, Y.Z. (2020). Towards large-size bulk ZIF-62 glasses via optimizing the melting conditions. J. Non-Cryst. Solids *530*, 119806. https://doi.org/10.1016/j.jnoncrysol.2019.119806.

Thorne, M.F., Gómez, M.L.R., Bumstead, A.M., Li, S., and Bennett, T.D. (2020). Mechanochemical synthesis of mixed metal, mixed linker, glass-forming metal–organic frameworks. Green Chem. *22*, 2505–2512. https://doi.org/10.1039/d0gc00546k.

To, T., Sorensen, S.S., Stepniewska, M., Qiao, A., Jensen, L.R., Bauchy, M., Yue, Y.Z., and Smedskjaer, M.M. (2020). Fracture toughness of a metal-organic framework glass. Nat. Commun. *11*, 2593. https://doi.org/10.1038/s41467-020-16382-7.

Wang, Y.H., Jin, H., Fin, H., Ma, Q., Mo, K., Mao, H.Z., Feldhoff, A., Cao, X.Z., Li, Y.S., Pan, F.S., and Jiang, Z.Y. (2020). A MOF glass

membrane for gas separation. Angew. Chem. Int. Ed. *59*, 4365–4369. https://doi.org/10.1002/ange.201915807.

Widmer, R.N., Lampronti, G.I., Anzellini, S., Gaillac, R., Farsang, S., Zhou, C., Belenguer, A.M., Wilson, C.W., Palmer, H., Kleppe, A.K., et al. (2019). Pressure promoted low-temperature melting of metal-organic frameworks. Nat. Mater. *18*, 370–376. https://doi.org/10.1038/s41563-019-0317-4.

Xiong, M., Li, N., Yin, G., Ching, W.-Y., and Zhao, X. (2020a). Effects of the halogenated imidazolate linker on the fundamental properties of amorphous zeolitic imidazolate frameworks. J. Non-Cryst. Solids *536*, 120005. https://doi.org/10.1016/j.jnoncrysol.2020.120005.

Xiong, M., Zhao, X., Yin, G., Ching, W.-Y., and Li, N. (2020b). Unraveling the effects of linker substitution on structural, electronic and optical properties of amorphous zeolitic imidazolate frameworks-62 (a-ZIF-62) glasses: a DFT study. RSC Adv. *10*, 14013–14024. https://doi.org/10.1039/c9ra09977h.

Yin, Z., Zhang, Y.B., Yu, H.B., and Zeng, M.H. (2020). How to create MOF glasses and take advantage of emerging opportunities. Sci. Bull. *65*, 1432–1435. https://doi.org/10.1016/j.scib.2020.05.003.

Zeng, M.H. (2021). Short-range disorder in MOF glasses. Natl. Sci. Rev. *8*, nwaa207. https://doi.org/10.1093/nsr/nwaa207.

Zhao, C.M., Dai, X.Y., Yao, T., Chen, W.X., Wang, X.Q., Wang, J., Yang, J., Wei, S.Q., Wu, Y.E., and Li, Y.D. (2017). Ionic exchange of metal organic frameworks to access single Nickel sites for efficient electroreduction of CO2. J. Am. Chem. Soc. *139*, 8078–8081. https://doi.org/10.1021/jacs.7b02736.

Zhou, C., Longley, L., Krajnc, A., Smales, G.J., Qiao, A., Erucar, I., Doherty, C.M., Thornton, A.W., Hill, A.J., Ashling, C.W., et al. (2018). Metal-organic framework glasses with permanent accessible porosity. Nat. Commun. *9*, 5042. https://doi.org/10.1038/s41467-018-07532-z.

STAR★METHODS

KEY RESOURCES TABLE

REAGENT or RESOURCE	SOURCE	IDENTIFIER
Deposited data		
ZIF-4 crystal structure	(Park et al., 2006)	CCDC code: VEJYUF
ZIF-62 crystal structure	(Thorne et al., 2020)	CCDC code: QUKGUB
Software and algorithms		
VASP 5.4.4	Hafner (2008)	https://www.vasp.at
Origin2022	OriginLab Corporation	https://www.originlab.com
Python 3	Python Software Foundation	https://www.python.org
VESTA	Momma and Izumi (2011)	http://jp-minerals.org/vesta/
VMD	Humphrey et al. (1996)	https://www.ks.uiuc.edu/Research/vmd/

RESOURCE AVAILABILITY

Lead contact

Further information and requests for resources and reagents should be directed to and will be fulfilled by the lead contact, Prof. Neng Li (lineng@whut.edu.cn).

Materials availability

This study did not generate new unique reagents.

Data and code availability

- All data reported in this paper will be shared by the lead contact upon request.
- The python Code we used in analyze of bond-length and bond-angles is written according to our output file which is pre-processing by Excel, which is not generally applicable to files of different formats. The code will be shared by the lead contact upon request.
- Any additional information required to reanalyze the data reported in this paper is available from the lead contact upon request.

EXPERIMENTAL MODEL AND SUBJECT DETAILS

(Omitted) Our study does not use experimental models typical in the life science.

METHOD DETAILS

In this work, all geometric structures in this study have been simulated by using Vienna Ab initio Simulation Package (VASP) (Hafner, 2008) in projector augmented wave (PAW) method (Blöchl, 1994), and the exchange-correlation energy was evaluated inthe Perdew–Burke–Ernzerhof (PBE) potential with the generalised gradient approximation (GGA) (Perdew et al., 1996), and the dispersion interactions were treated at the DFT-D3 (Grimme et al., 2010). Due to a large primitive cell consist of 300 atoms and the dimensions up to 20 Å, we consider that single K-point at the zone center is sufficient for the boundary condition of such large structure model. The high energy cut-off of 400 eV was used with the electronic convergence criterion set at 10^{-4} eV. For the ionic relaxation, we set the force convergence criteria to be 2×10^{-3} eV $Å^{-1}$.

All simulations were performed under the canonical ensemble, that is, the number of particles, the temperature and volume are fixed (NVT). The temperature was controlled by the Nose-Hoover thermostat (Hoover, 1985; Nosé, 1984). According to the vibration frequency of the C-H bond in ZIFs, a time-step of 0.5 fs was used in the AIMD runs. We conducted the heating simulations from 300 K starting from the crystalline structure in 10 ps to get the pre-equilibrium model. Afterward, we carry out the NVT equilibria for 15–20 ps at 300, 600, 900, 1200, and 2000K, and analyzed the balancing process of the last 5–10 ps. To test for

statistical errors, we performed longer kinetic tests on ZIF-62 up to 60 ps at 2000 K. We averaged sampling at 5 ps intervals and characterised the variability by PRDF of Zn-N. The results are in Figure S3. The test results show no significant deviation from the ZIF-62 structure after 10 ps suggesting that systematic errors can be controlled in our adopted approach.

To investigate the pre-melt and melting structure, we used 20 snapshots in each of the equilibrium structures at the respective temperature, and subsequently, the averaging procedure was obtained. The atomic structures were constructed using the VESTA code (Momma and Izumi, 2011). VMD code (Humphrey et al., 1996) and python were used to analyze trajectory files and structural characteristics. The initial structure of ZIF-4 and ZIF-62 are in consistent with previous studies by other groups. The optimized unit cell of ZIF-62 contains 320 atoms and *Pbca* space group with the cell parameters a = 14.91 Å, b = 17.49 Å, c = 19.08Å and $\alpha = \beta = \gamma = 90^{\circ}$. The optimized unit cell of ZIF-4 contains 272 atoms and Pbca space group with the cell parameters a = 15.39 Å, b = 15.30 Å, c = 18.42Å and $\alpha = \beta = \gamma = 90^{\circ}$. The coordination number of N atoms around the Zn atoms is computed by taking a cut-off radius of 2.5 Å, a value chosen from the Zn–N partial radial distribution function at room temperature.

In describing the amorphous and glass-forming abilities of crystals ZIFs, ZIFs are treated as network structures consisting of Zn, C, and N atoms. The corresponding parameters X and Y in Figure 7 are taken from the pair radial distribution functions (PRDF) of the respective crystals for Zn - (C, N) pairs. For crystal ZIFs, the distribution of peaks in the PRDF is isolated, as shown in Figure S4. For the first five peaks, the peak position and height were recorded for each peak, noted as (x_i, Pi). For each ZIF, $X = x_5 - x_1$, Y=(P1+P2+P3+P4+P5)/P1.

QUANTIFICATION AND STATISTICAL ANALYSIS

(Omitted) Our study does not include statistical analysis or quantification.

ADDITIONAL RESOURCES

(Omitted) Our study has not generated or contributed to a new website/forum.